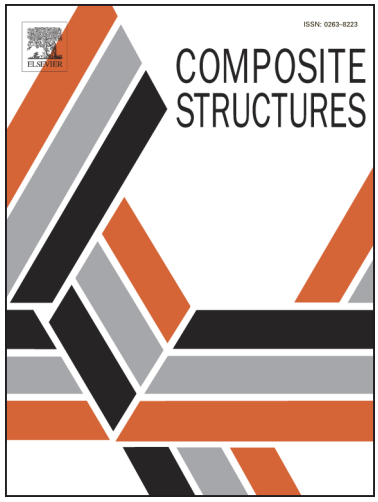

3D FEA Modelling of Laminated Composites in Bending and Their Failure Mechanisms

M. Meng, H.R. Le, M.J. Rizvi, S.M. Grove

PII: S0263-8223(14)00496-6
DOI: http://dx.doi.org/10.1016/j.compstruct.2014.09.048
Reference: COST 5924

To appear in: *Composite Structures*

Please cite this article as: Meng, M., Le, H.R., Rizvi, M.J., Grove, S.M., 3D FEA Modelling of Laminated Composites in Bending and Their Failure Mechanisms, *Composite Structures* (2014), doi: http://dx.doi.org/10.1016/j.compstruct.2014.09.048

3D FEA Modelling of Laminated Composites in Bending and Their Failure Mechanisms

M. Meng*, H. R. Le, M. J. Rizvi, S. M. Grove

School of Marine Science and Engineering, Plymouth University, United Kingdom

*Fax: +44 (0)1752 586101; email address: maozhou.meng@plymouth.ac.uk

Abstract

This paper developed three-dimensional (3D) Finite Element Analysis (FEA) to investigate the effect of fibre lay-up on the initiation of failure of laminated composites in bending. Tsai-Hill failure criterion was applied to identify the critical areas of failure in composite laminates. In accordance with the 3D FEA, unidirectional ($[0]_{16}$), cross-ply ($[0/90]_{4s}$) and angle-ply ($[\pm45]_{4s}$) laminates made up of pre-preg Carbon Fibre Reinforced Plastics (CFRP) composites were manufactured and tested under three-point bending. The basic principles of Classical Laminate Theory (CLT) were extended to three-dimension, and the analytical solution was critically compared with the FEA results. The 3D FEA results revealed significant transverse normal stresses in the cross-ply laminate and in-plane shear stress in the angle-ply laminate near free edge regions which are overlooked by conventional laminate model. The microscopic images showed that these free edge effects were the main reason for stiffness reduction observed in the bending tests. The study illustrated the significant effects of fibre lay-up on the flexural failure mechanisms in composite laminates which lead to some suggestions to improve the design of composite laminates.

Keywords: 3D, FEA, laminate, flexural, CLT

1. Introduction

Laminated composites have been widely used in renewable energy devices such as wind turbines [1] and underwater turbines [2] which are usually subjected to a combination of tension, bending and twisting. Delamination plays an important role in the composites failure, while one of the main causes of composites delamination is the interlaminar shear stress [3]. Many theories have been developed to predict the distribution of interlaminar shear stress in composite laminates. It is well-known that Classical Laminate Theory (CLT) [4], First-order Shear Deformation Theory (FSDT) [5, 6] and Refined Shear Deformation Theory (RSDT) [7] give a good prediction of mechanical behaviour with infinite composite plates. However, these classical theories based on infinitely wide plates have experienced difficulties on regions near boundaries [8, 9]. This is because these methods consider the laminated composites as shell elements which ignore the effects of the thickness of the component. The shell method suffers from poor accuracy in case of high ratio of height to width.

Three-dimensional numerical analysis has been used to examine the stress distribution in laminated composites. The pioneer work was carried out by Pipes and Pagano using the Finite Difference Method (FDM) [10, 11]. They demonstrated the singularity of interlaminar shear stress at the edge region in an angle-ply laminate under tensile stress. Similar work investigated the interlaminar shear stress at free edges using FEA [12-14], Eigen-function expansions [15, 16], Boundary Layer theory (BLT) [17, 18], and Layer-wise theory (LWT) [19]. A good review by Kant et al [20] has covered the analytical and numerical methods on free-edge problems of interlaminar shear stress up to year 2000.

Previous work on 3D analysis has illustrated the increase of interlaminar shear stress at the edge region. Although the global load may be lower than the composites strength, the interlaminar shear stress can induce the initial delamination at edge region which will reduce the fatigue life of composites. This phenomenon has been reported in composites design and manufacturing [21]. In order to investigate the free edge effect on interlaminar shear stress, most of the previous works were focused on the uniform axial loads. This type of loading condition does not induce some stress components, such as out-of-plane stresses, which nevertheless have a significant effect on the bending failure behaviour. Moreover, with the decrease of the support span in bending, these stress components play an increasingly important role in composite failure modes. Due to the nature of bending, laminates are subjected to tension, compression and shear, so all of the six stress components should be

considered when evaluating failure criteria. However, there have been few reports on the free edge effect in bending.

Due to the limitation of computing power, earlier works on 3D analysis could only consider a few plies for the demonstration. When composite laminates are made of many plies with complicated orientation, the prediction of these models may lead to inaccurate results. Pipes and Pagano[10] illustrated the singularity of interlaminar shear stress at edge region of an angle-ply laminate which consisted of four plies, however, this singularity is unlikely to occur in a laminate with many plies shown in the present work. Additionally, the FEA model for angle-ply laminate is unlikely to be simplified as symmetric in bending, due to the complicated ply lay-up pattern. This means that a full model need to be considered and significant computing resources are required for modelling.

The present work was intended to understand how the fibre lay-up affects the initiation of failure of laminated composites in bending. A series of composites with 3 common lay-up sequences were manufactured and tested in bending following ISO standards[22, 23] to measure the critical failure loads and failure modes. A robust 3D FEA and an extended CLT model were then applied to examine the stress distribution under the measured failure loads. The stress distribution in critical areas of the laminated composites were examined and correlated with the observation of the initiation of failure in experiments.

2. Laminate preparation

Three different lay-ups of laminates were investigated for the distributions of flexural and interlaminar shear stress. Table 1 shows the laminate configuration. These three lay-up (unidirectional $[0]_{16}$, cross-ply $[0/90]_{4s}$ and angle-ply $[\pm45]_{4s}$) are the simplest examples of laminates which show a range of behaviour. The stress distributions and failure modes for a given laminate lay-up could be extended in this direction. All of the laminates were made up of 16 layers of high strength carbon fibre/epoxy pre-preg (Cytec 977-2-35-12KHTS-134-150). The pre-preg plates were placed on a mould and sealed in a vacuum bag, and then were autoclave-cured at 0.6 MPa pressure. A heating rate of 3˚C/min from room temperature to 180˚C was applied, and then the pre-preg plates were held at 180˚C for 120 minutes and cooled at room temperature. For the cross-ply laminate, the bottom and top plies were set as the longitudinal fibre orientation; therefore its flexural modulus was higher than tensile modulus. The angle-ply laminate and cross-ply laminate were cut from the same composite

panel, with different cutting directions. In order to make the laminate 'self-balance', the middle two plies were set at the same fibre orientation.

Table 1 Laminate configuration

Laminate	Lay-up	Thickness(mm)	Ply-thickness(mm)
Unidirectional	$[0]_{16}$	2.08	0.13
Cross-ply	$[0/90]_{4s}$	1.92	0.12
Angle-ply	$[\pm45]_{4s}$	1.92	0.12

The final thicknesses of the three manufactured plates were not the identical. There are probably two reasons: a) the unidirectional laminate has a rougher surface than cross-ply laminate; b) the void content in unidirectional laminate is slightly higher than that in cross-ply laminate. Hypothesis a) may lead to a thicker laminate, since the dimension was measured by a digital vernier calliper. Hypothesis b) was confirmed by microscope image. Figure 1 shows a void in microscope image of cross-section of unidirectional laminate. However, no voids were found in cross-ply and angle-ply laminates. In accordance with the actual thicknesses of the laminates, the ply thicknesses of unidirectional and cross-ply laminates were adjusted in CLT and FEA models for consistency (shown in Table 1).

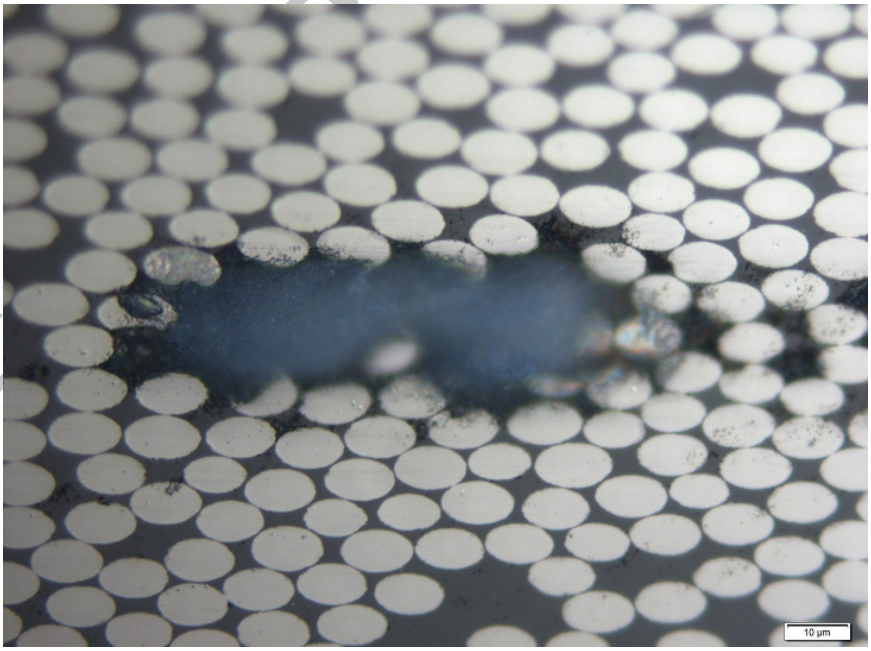

Figure 1 Optical microscope image of unidirectional laminate. A huge void was found, which was probably because of the manufacturing process.

The flexural stress was measured by the long-beam method [24] with the dimension of $length \times width = 100mm \times 15mm$, while the interlaminar shear stress was measured by the short-beam method [25] with the dimension of $length \times width = 20mm \times 10mm$.

3. Bending test results

The experiment was conducted according to ISO standards [24, 25] using three-point bending. At least five samples in each group were tested and the mean values were calculated. The results are shown in Table 2.

Table 2 Experimental results from three-point bending tests and the Standard Deviations (SDs)

laminate	Unidirectional $[0]_{16}$		Cross-ply $[0/90]_{4s}$		Angle-ply $[\pm45]_{4s}$
Groups	**Long beam**	**Short beam**	**Long beam**	**Short beam**	**Short beam**
Length (mm)	100	20	100	20	20
Width (mm)	15.18±0.03	10.14±0.03	15.08±0.02	10.14±0.10	10.10±0.12
Height (mm)	2.09±0.06	2.13±0.07	1.93±0.01	1.94±0.02	1.93±0.01
Span (mm)	80	10	79	10	10
$F_{\max}$ **(N)**	853±32	2933±126	630±21	2257±83	1395±61
$D_{\max}$ **(mm)**	6.59±0.27	—	8.99±0.31	—	—
E_{app}^{f} **(GPa)**	120±3.1	—	79.7±0.8	—	—
σ_x^{app} **(MPa)**	1544±49	—	1328±39	—	—
$(\sigma_x^{app})_{cor}$ **(MPa)**	1598±56	—	1421±48	—	—
τ_{xz}^{app} **(MPa)**	—	101.9±3.5	—	86.1±4.0	53.7±2.8

$F_{\max}$ -maximum flexure load; $D_{\max}$ -maximum deflection; E_{app}^{f} -apparent flexural modulus; σ_x^{app} -apparent flexural strength; $(\sigma_x^{app})_{cor}$ -apparent flexural strength with 'large-deformation' correction; τ_{xz}^{app} -apparent interlaminar shear strength.

The value $D_{\max}/L$ of unidirectional laminate was about 8%, as shown in Table 2, which was close to the 'large-deflection criterion' (10%) [24]. Therefore, the flexural strength of unidirectional laminate was calculated by 'large-deflection correction',

$$\left(\sigma_{\max}^{f}\right)_{cor} = \frac{3F_{\max}L}{2wh^2}\left(1+6\left(\frac{D_{\max}}{L}\right)^2-3\left(\frac{D_{\max}h}{L^2}\right)\right) \quad (1)$$

4. Methodologies

4.1 FEA approach

The technical term 'symmetry' includes symmetry in geometry, material and boundary condition. Although the lay-up sequence (as well as geometry) is symmetric for all specimens shown in Table 1, the angle-ply laminate has no through-thickness plane of symmetry in term of material orientation.

All of the specimens were 'simply supported', which presents a linear relationship between flexure load and deflection. The loads applied in the FEA models (Table 3) were taken as the maximum measured loads in the three-point bending tests.

Table 3 Loading forces in different groups of coupons

Orientation	Unidirectional		Cross-ply		Angle-ply
Groups	Long beam	Short beam	Long beam	Short beam	Short beam
Force (N)	853	2933	630	2257	1395

In the 3D FEA model, the boundary conditions are quite different from a 2D model, and some modelling techniques should be introduced because the 'simply supported' and loading boundary conditions might lead to inaccurate results due to the stress concentration at these boundaries. Additionally, the 'contact' boundary condition is not appropriate in present work, so that these have been replaced by distributed loads with sinusoidal distribution, which includes an downward (negative) distributed load (P) in the middle area of top surface (load-point) and half of an upward (positive) distributed load ($P/2$) at the left and right ends of bottom surface, as shown in Figure 2. For the long-beam specimens, the spans (L) were set as 80mm (longitudinal laminate) and 79mm (cross-ply laminate), while the short-beam specimens had a span of 10mm.

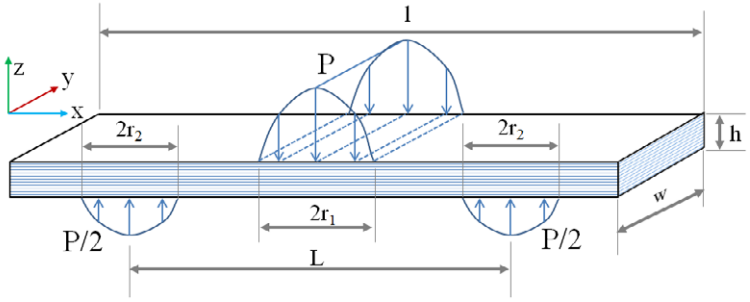

Figure 2 Modelling conditions were equal to testing conditions. The two 'simply supported' boundary conditions at two ends were replaced by positive distributed loads ($P/2$).

In order to avoid rigid movement, some assistant boundary conditions were applied to eliminate the six degree of freedom (DOF). With the natural symmetry of unidirectional laminate and cross-ply laminate, two symmetric planes were applied to eliminate the DOFs of x, y, and the rotation about three axes. The two central points at each end of the laminate (z=h/2) were restrained as z=0 to eliminate the last DOF. However, the 'symmetric plane' boundary conditions do not exist in angle-ply laminate, due to the asymmetric material properties. Two 'edge displacement' boundary conditions were applied to replace the symmetric planes for eliminating the DOFs. Figure 3 shows the artificial boundary conditions for the DOFs elimination in unidirectional and cross-ply laminates (a), and angle-ply laminate (b).

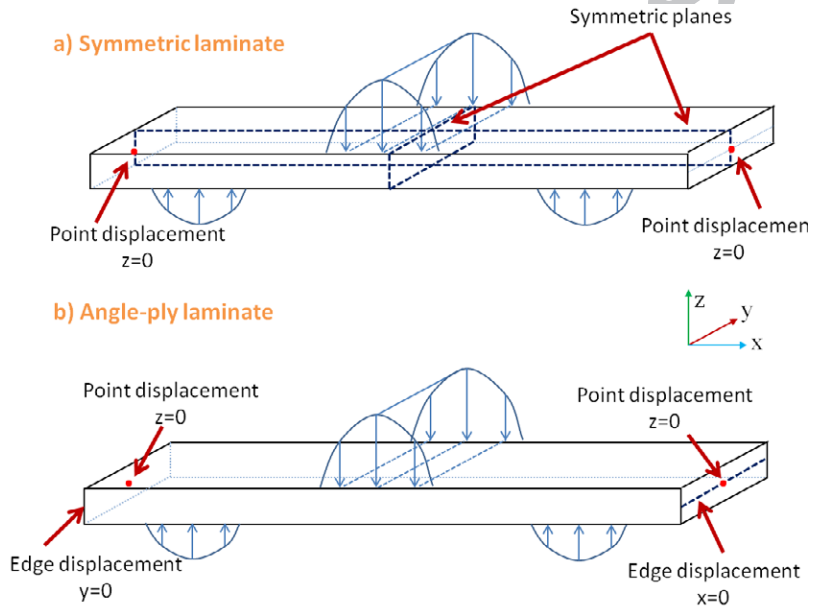

Figure 3 Boundary conditions applied in a) symmetric laminates and b) angle-ply laminate

The properties of carbon fibre (HTS) and epoxy (977-2) were used in FEA models. Table 4 gives the material properties of pre-preg CFRP composite from the manufacturers' data sheets [26, 27]. It can be seen from Table 4 that the flexural strength of the matrix is much higher than the tensile strength. This may affect the transverse strength of composite lamina. The fibre volume fraction can be calculated from W_m ,

$$V_f = \frac{(1 - W_m)/\rho_f}{(1-W_m)/\rho_f + W_m/\rho_f} = \frac{\rho_m(1-W_m)}{\rho_m(1-W_m)+\rho_f W_m} \qquad (2)$$

Substituting the values in Table 4 into equation (2), the fibre volume fraction can be estimated as $V_f = 57.9\%$.

Table 4 Material properties of fibre and matrix. The fibre transverse modulus is estimated as 10% of its longitudinal modulus, according to references[28-30]

Symbol	E_1^f	$E_2^f = E_3^f$	$\nu_{12}^f = \nu_{13}^f$	ν_{23}^f	ρ_f	ρ_m
Value	238GPa	23.8GPa	0.2	0.4	1.77 gcm^{-3}	1.31 gcm^{-3}
Symbol	W_m*	E_m	ν_m	$(\sigma_f^{ult})^t$	$(\sigma_m^{ult})^t$	$(\sigma_m^{ult})^f$
Value	35%	3.52GPa	0.34	4.3GPa	81.4 MPa	197MPa

***W_m is the matrix fraction in weight; $(\sigma_f^{ult})^t$ and $(\sigma_m^{ult})^t$ are the tensile strength of fibre and matrix; $(\sigma_m^{ult})^f$ is flexural strength of matrix.**

Employing the 'rule of mixture' [31] and 'Halpin & Tsai' [32] methods, the in-plane material properties of lamina can be calculated. However, there is no agreed formula to calculate the transverse material properties (ν_{23}, G_{23}). In the present work, the transverse Poisson's ratio was evaluated by the hydrostatic assumption as shown in Appendix I. For the orthotropic material, such as composite laminate, Tsai-Hill failure criterion [33, 34] has shown a good fit to experiments, and this is used in the present work:

$$(G_2+G_3)\sigma_1^2+(G_1+G_3)\sigma_2^2+(G_1+G_2)\sigma_3^2-2(G_3\sigma_1\sigma_2+G_2\sigma_1\sigma_3+G_1\sigma_2\sigma_3-G_4\tau_{23}^2-G_5\tau_{13}^2-G_6\tau_{12}^2)<1 \quad (3)$$

$$G_1=\frac{1}{(\sigma_2^{ult})^2}-\frac{1}{2(\sigma_1^{ult})^2}, G_2=G_3=\frac{1}{2(\sigma_1^{ult})^2}, G_4=\frac{1}{2(\tau_{23}^{ult})^2}, G_5=\frac{1}{2(\tau_{13}^{ult})^2}, G_6=\frac{1}{2(\tau_{12}^{ult})^2} \quad (4)$$

There are six parameters of lamina strength in equations (3 & 4), however only four are independent ($\sigma_2^{ult}=\sigma_3^{ult}$, $\tau_{12}^{ult}=\tau_{13}^{ult}$). The longitudinal tensile strength of lamina $(\sigma_1^{ult})^t$ can be evaluated by the 'maximum strain' method [31]; $(\sigma_2^{ult})^t$ is assumed to be the transverse flexural strength of the lamina, which was separately obtained by three-point bending test of $[90]_{16}$ samples; the shear strength τ_{13}^{ult} is estimated by the interlaminar shear test of $[0]_{16}$ samples, which is shown in Table 2; τ_{23}^{ult} is assumed to be the same as the shear strength of matrix, which is in the order of 6% (ultimate shear strain)[35].

Substituting the material properties of fibre and matrix in Table 4, all the material properties of lamina required by FEA software were calculated, as shown in Table 5.

Table 5 Material properties of lamina for simulation

Symbol	E_1	$E_2 = E_3$	$G_{12} = G_{13}$	G_{23}	$\nu_{12} = \nu_{13}$	ν_{23}
Value	139GPa	8.8GPa	4.7GPa	3.0GPa	0.26	0.48
Symbol	$(\sigma_1^{ult})^t$	$(\sigma_1^{ult})^c$	$(\sigma_2^{ult})^t = (\sigma_3^{ult})^t$	$(\sigma_2^{ult})^f$	$\tau_{12}^{ult} = \tau_{13}^{ult}$	τ_{23}^{ult}
Value	2.52GPa	1.58GPa*	123MPa	123MPa	102MPa	79MPa

***The longitudinal compressive strength of the lamina $(\sigma_1^{ult})^c$ is estimated by reference [26], which used the same matrix and a similar fibre to the present work.**

It is important to note that two coordinate systems are employed: a) the local coordinate system represents stress or strain in the lamina level (subscripts 1, 2, and 3), and b) the global coordinate system represents stress and strain at the laminate level (subscripts x, y, and z). The failure criterion must be applied in local coordinate system. For example c_x, c_y and τ_{xy} are based on global coordinates, which should be transformed to the local coordinates (c_1, c_2 and τ_{12}) in accordance with the failure criterion.

Orthotropic material properties were applied in the simulation and every off-axis ply used a rotated coordinate,

$$\begin{pmatrix} x \\ y \end{pmatrix} = \begin{bmatrix} \cos\theta & -\sin\theta \\ \sin\theta & \cos\theta \end{bmatrix} \begin{pmatrix} X \\ Y \end{pmatrix} \tag{5}$$

where X and Y are the transformed variables in the rotated (θ) coordinate system. The elastic properties of lamina (Young's modulus, Shear modulus and Poisson's ratio) were transformed using Equation (5) for the definition of FEA.

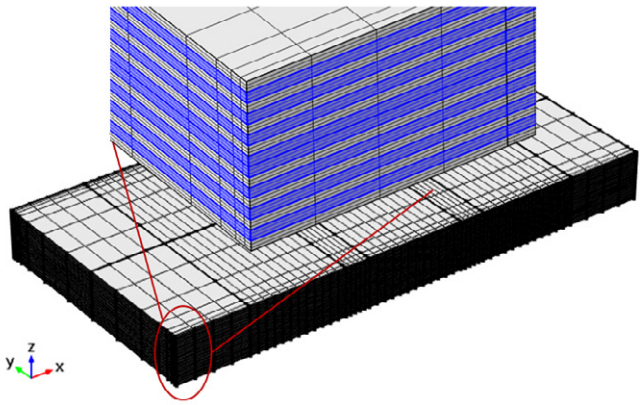

Figure 4 Mesh plot of $20mm \times 10mm$ laminate with local refinement. The edge area was refined to investigate the free edge effect.

In FEA models, all of the 16 plies were built as 3D-solid element, and bonded together. Because the mesh quality could affect the 3D FEA results significantly, two methods for mesh quality control were employed: a) distributed mesh was defined near edge region; b) global elements were referred to 'q' factor, which was evaluated by [36],

$$q = \frac{24\sqrt{3}V}{\left(\sum_{i=1}^{12} h_i^2\right)^{3/2}} \tag{6}$$

where V is the volume, and h_i are the edge lengths. If $q > 0.1$, the mesh size should not affect the solution quality.

The through-thickness mesh density has a weak influence on the FEA results since the material properties within each ply are considered as homogeneous. However the mesh quality in the width direction has to be refined and the dimension of an individual element at the edge should be comparable to the ply thickness. In the present work, geometry near the edge was refined to be approximately one half-ply thickness along the width, and each ply was divided into 3 elements through-thickness, as shown in Figure 4. A finer mesh than this would not provide noticeable improvement of the FEA solution, while demanding exponentially increasing computing resources. Figure 5 shows the relationship between the mesh size (multiple of one-ply thickness) and the solution. The 3D FEA models were solved by COMSOL Multiphysics[36], with approximate one million DOFs in each laminate.

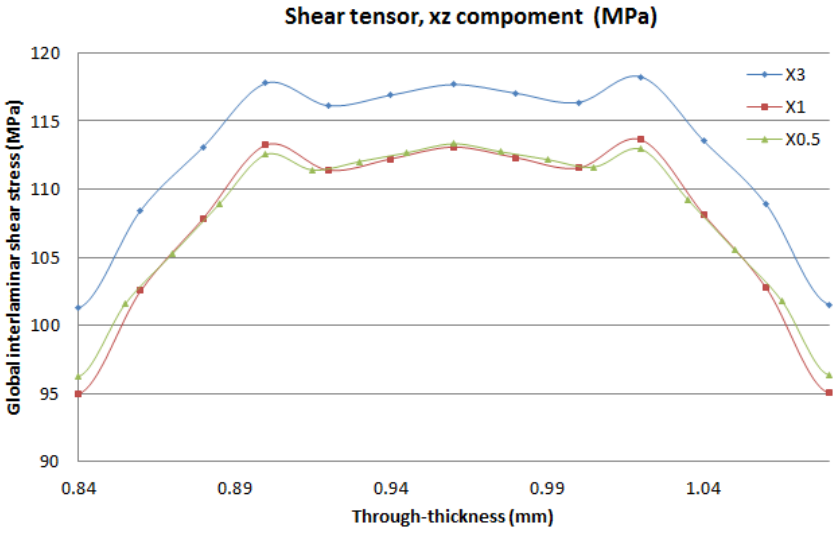

Figure 5 The effect of mesh size near the edge region on the distribution of global interlaminar shear stress in short-beam angle-ply laminate. The results show that 0.5 was sufficient to get mesh independency.

4.2 3D CLT formulae

A 3D formulation of CLT is required to extract the six stress components in laminates. The formulae are shown in Appendix II. In the 2D version of CLT, the transverse shear stresses are neglected. It would be reasonable if the span is long enough and the width is infinite. In the present work, these transverse stress components are compared with 3D FEA models. With the 3D version of $[a,b;b,d]$ matrix, the interlaminar shear stress τ_{xz} and transverse shear stress τ_{yz} can be evaluated by the principle of continuum mechanics [37],

$$\begin{aligned}\tau_{xz}^{(k)} &= \sum_{j=1}^{k-1}\int_{z_{j-1}}^{z_j}\left(\frac{\partial \tau_{xz}}{\partial z}\right)_{(j)}dz + \int_{z_{k-1}}^{z}\left(\frac{\partial \tau_{xz}}{\partial z}\right)_{(k)}dz \\ &= -\sum_{j=1}^{k-1}\left\{\begin{array}{l}\left(\overline{C}_{11(j)}b_{11}+C_{12(j)}b_{21}+\overline{C}_{16(j)}b_{61}\right)\left(z_j-z_{j-1}\right)\\ +\frac{1}{2}\left(\overline{C}_{11(j)}d_{11}+\overline{C}_{12(j)}d_{21}+\overline{C}_{16(j)}d_{61}\right)\left(z_j^2-z_{j-1}^2\right)\end{array}\right\}Q_x - \left\{\begin{array}{l}\left(\overline{C}_{11(k)}b_{11}+\overline{C}_{12(k)}b_{21}+\overline{C}_{16(k)}b_{61}\right)\left(z-z_{k-1}\right)\\ +\frac{1}{2}\left(C_{11(k)}d_{11}+\overline{C}_{12(k)}d_{21}+\overline{C}_{16(k)}d_{61}\right)\left(z^2-z_{k-1}^2\right)\end{array}\right\}Q_x\end{aligned} \tag{7}$$

$$\begin{aligned}\tau_{yz}^{(k)} &= \sum_{j=1}^{k-1}\int_{z_{j-1}}^{z_j}\left(\frac{\partial \tau_{yz}}{\partial z}\right)_{(j)}dz + \int_{z_{k-1}}^{z}\left(\frac{\partial \tau_{yz}}{\partial z}\right)_{(k)}dz \\ &= -\sum_{j=1}^{k-1}\left\{\begin{array}{l}\left(\overline{C}_{61(j)}b_{11}+C_{62(j)}b_{21}+\overline{C}_{66(j)}b_{61}\right)\left(z_j-z_{j-1}\right)\\ +\frac{1}{2}\left(\overline{C}_{61(j)}d_{11}+\overline{C}_{62(j)}d_{21}+\overline{C}_{66(j)}d_{61}\right)\left(z_j^2-z_{j-1}^2\right)\end{array}\right\}Q_x - \left\{\begin{array}{l}\left(\overline{C}_{61(k)}b_{11}+\overline{C}_{62(k)}b_{21}+\overline{C}_{66(k)}b_{61}\right)\left(z-z_{k-1}\right)\\ +\frac{1}{2}\left(C_{16(k)}d_{11}+\overline{C}_{26(k)}d_{21}+\overline{C}_{66(k)}d_{61}\right)\left(z^2-z_{k-1}^2\right)\end{array}\right\}Q_x\end{aligned} \tag{8}$$

The local interlaminar shear stress in the k^{th} ply (along fibre orientation) is evaluated according to its orientation,

$$\begin{aligned}\tau_{13}^{(k)} &= \tau_{xz}^{(k)}\cos\theta_{(k)} + \tau_{yz}^{(k)}\sin\theta_{(k)} \\ \tau_{23}^{(k)} &= -\tau_{xz}^{(k)}\sin\theta_{(k)} + \tau_{yz}^{(k)}\cos\theta_{(k)}\end{aligned} \tag{9}$$

Table 6 Maximum ply normal stress and interlaminar shear stress by 3D CLT

Orientation	**Unidirectional $[0]_{16}$**		**Cross-ply $[0/90]_{4s}$**		**Angle-ply $[\pm45]_{4s}$**	**Notes**
Groups	**Long beam**	**Short beam**	**Long beam**	**Short beam**	**Short beam**	
E_{CLT}^{f} **(GPa)**	139	—	86.5	—	—	Flexural modulus by CLT
$\sigma_1^{\max}$ **(MPa)**	1598±56	—	2157±78	—	—	Maximum ply normal stress
$\tau_{13}^{\max}$ **(MPa)**	—	101.9±3.5	—	83.3±2.6	40.6±2.1	Maximum ply interlaminar shear stress

Substituting the laminate dimension, flexure loads and deflections in Table 2 into 3D CLT formulae, the maximum ply normal stress and interlaminar shear stress can be obtained, as shown in Table 6. In order to process the data, a MATLAB program [38] was developed.

5. Results and discussion

5.1 Unidirectional laminates

For the long-beam method, the ISO standard considers the flexural stress in longitudinal direction by neglecting the other components. According to the 3D FEA model, the stress components c_2 and c_3 are very small compared with c_1 (about 2%) because of the 'simply supported' boundary condition. The flexural stress c_1 shows a tiny increase (about 2%) near the free edge region, as shown in Figure 6. Although the maximum tensile stress is much lower than longitudinal tensile strength $(\sigma_1^{ult})^t$ (2.52GPa), the compressive stress is very close to the compressive strength $(\sigma_1^{ult})^c$ (1.58GPa), as shown in Table 5. Therefore, the long-beam unidirectional laminate failed in compression, rather than tension.

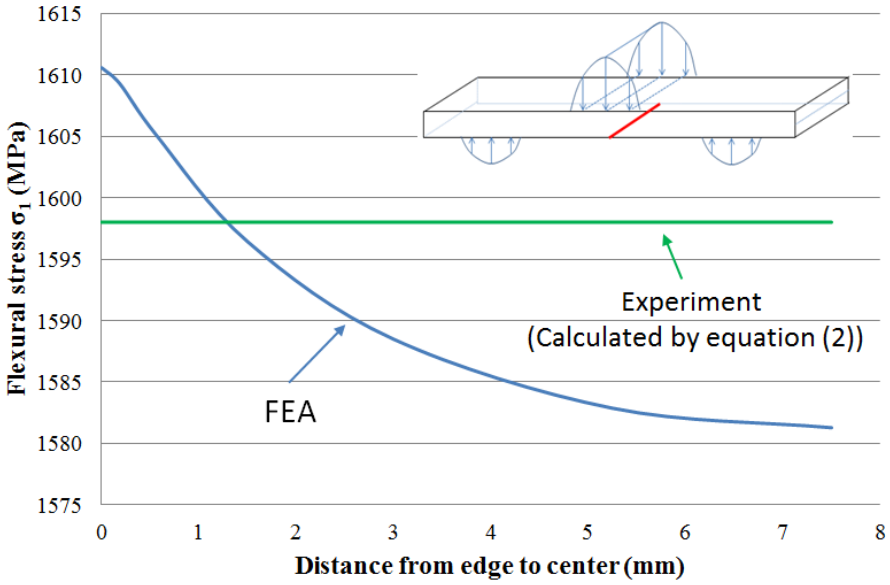

Figure 6 Distribution of tensile stress c_1 on bottom surface of long-beam unidirectional laminate. The stress (FEA) shows a minor fluctuation about 2% between the free edge and central areas.

The microscope observation confirmed this hypothesis. Figure 7 shows a typical failure image of long-beam unidirectional laminate, and Figure 8 shows the deflection-load curves of long-beam unidirectional laminate. Figure 7 (b) clearly shows the interface between tensile and compressive failures within a unidirectional laminate, while Figure 7 (c) indicates that fibres in the upper half failed by compression. A survey of literature [39-42] shows that the half-wavelength λ_0 of fibre microbuckling is typically 10-15 times of fibre diameter, which is in accordance with the kinking band shown in Figure 7 (b).

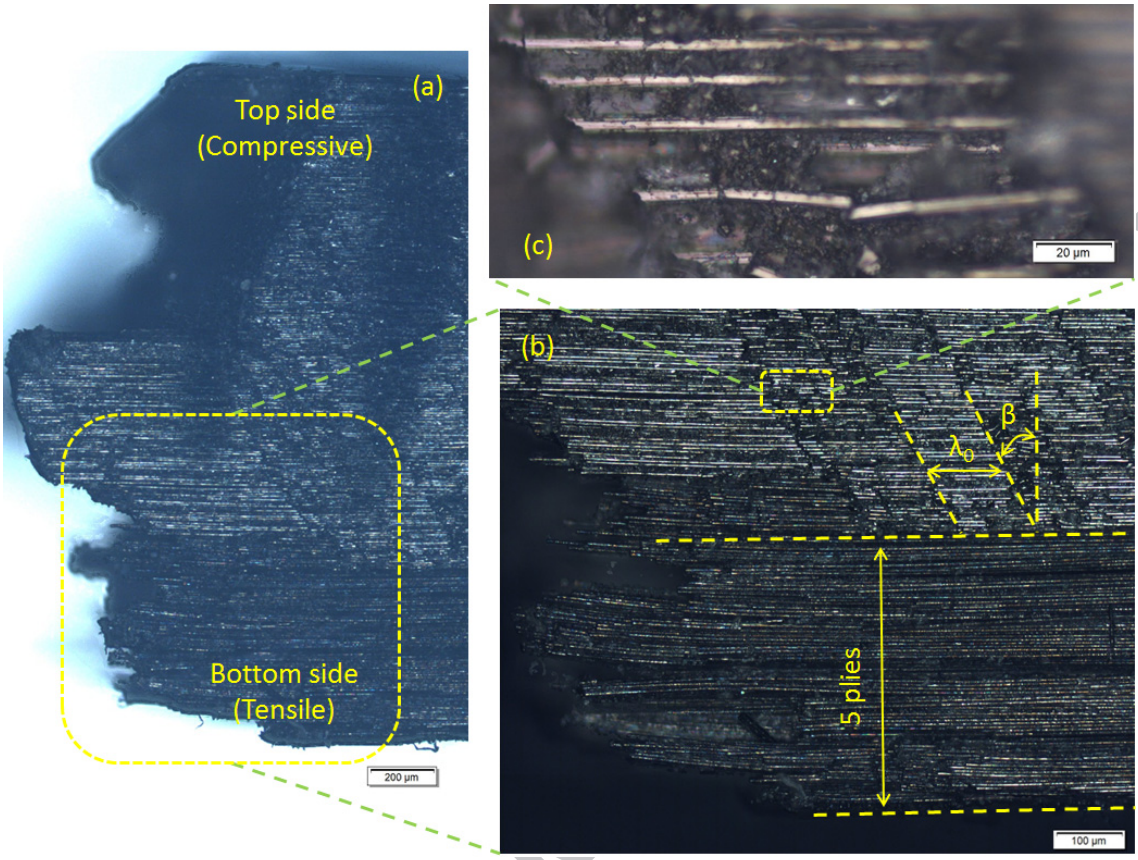

Figure 7 Microscope image of failure mode in a long-beam unidirectional laminate under three-point bending (side-view). Approximate 70% of the plies failed by compression, and fibre microbuckling could be observed on the compressive side.

The observed stiffness dropped in small steps when the flexure load reached the peak, and each step of 'stiffness losses' represents the failure of a single ply (compressive failure). The flexural stress re-distributed, and the lower plies withstood the maximum compressive stress but the tensile stress at bottom ply did not reach the tensile strength. As a consequence, more and more plies failed by compressive stress, and then the sample broke into two parts suddenly when the last 1/3 of the plies failed. Previous literature [39-41, 43] shows that the longitudinal compressive strength of unidirectional laminate is about 60%~70% of its tensile strength. One possible reason is that fibre misalignment causes fibre microbuckling. Figure 9 is a schematic diagram to show the microbuckling in long-beam unidirectional laminate. The carbon fibres are allowed to buckle into the weaker resin in lower plies and finally break under in-plane compressive stress.

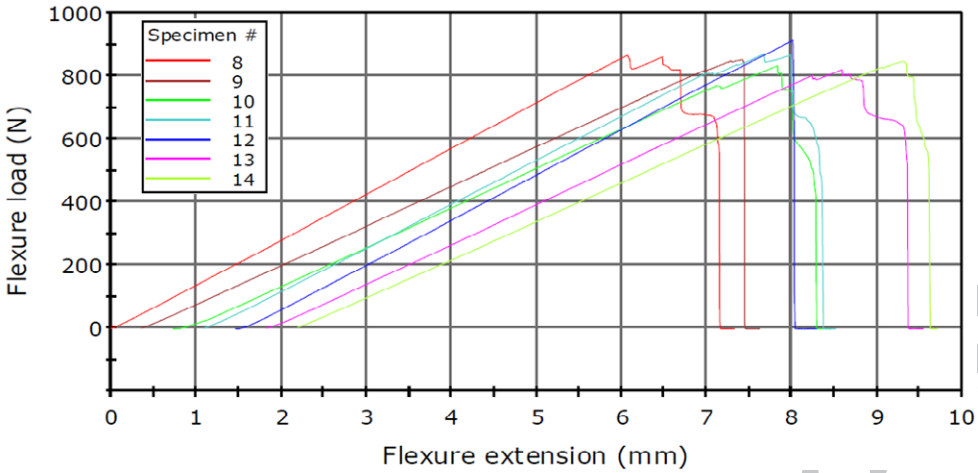

Figure 8 Deflection-load curves of long-beam unidirectional laminate under three-point bending. Laminate failed rapidly after the first 'stiffness losses' appeared (progressive failure is beyond the scope of this paper).

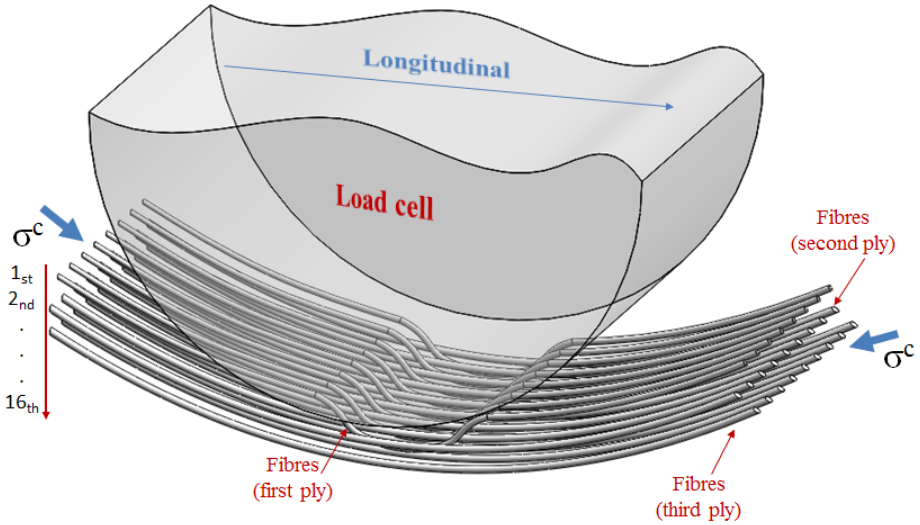

Figure 9 Schematic diagram of fibre microbuckling of long-beam unidirectional laminate. With the same fibre orientation, the second ply is likely to 'buckle' following the first ply by the compressive stress, and then followed by the third ply, and so on.

For the short-beam laminate, the 3D FEA model shows a significant increase (15%) of free edge effect on the interlaminar shear stress τ_{13}. However this value decays sharply inside the laminate and then converges to the CLT value (c.f. Table 6) in the central area, as shown in Figure 10. This implies that the laminate failed initially from edge area. Additionally, due to the short span, the out-of-plane normal stress c_3, which is neglected in the ISO standard, shows a relatively high value in the FEA model. Similarly, this value decays inside the laminate, and is located at the loading area. Figure 11 shows the distribution of out-of-plane normal stress c_3 and typical failure images of the short-beam unidirectional laminate. The

maximum out-of-plane normal stress c_3 is very close to the transverse tensile strength $\left(\sigma_2^{ult}\right)^t$ in Table 5. It also indicates that the ISO standard may underestimate the interlaminar shear strength of short-beam unidirectional laminate.

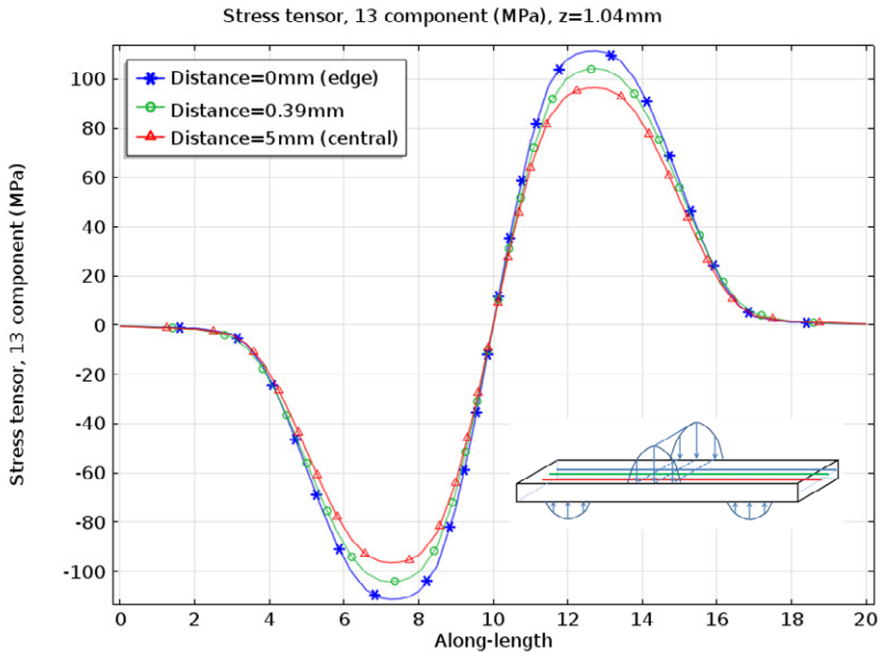

Figure 10 Distribution of interlaminar shear stress τ_{13} on middle plane of short-beam unidirectional laminate. The higher value at free edge region implies the crack could be initialized from this area.

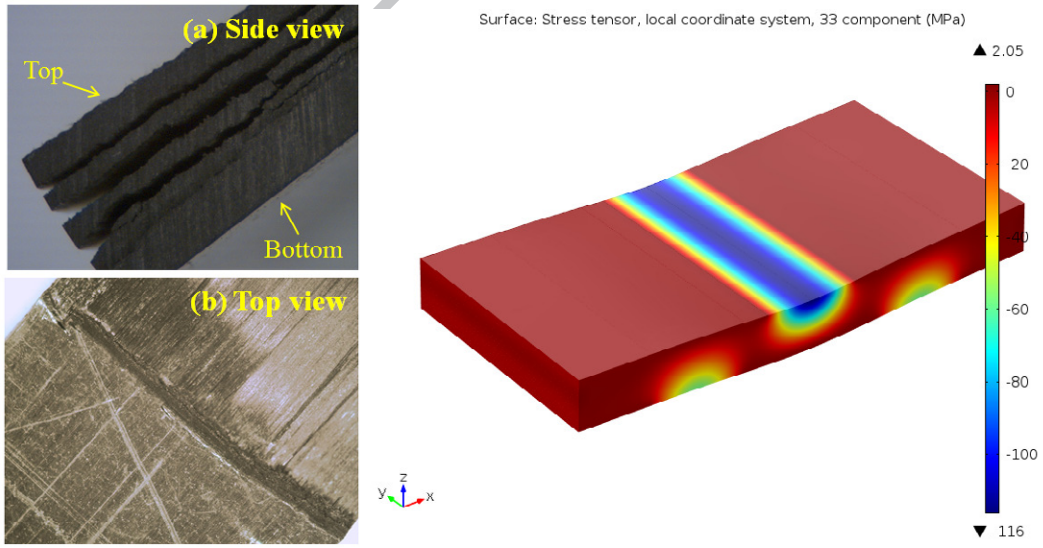

Figure 11 Typical failure images of short-beam unidirectional laminate and the distribution of out-of-plane normal stress c_3. The combination of interlaminar shear stress τ_{13} and out-of-plane normal stress c_3 leads to delamination at compressive (top) part of the laminate.

5.2 Cross-ply laminates

Because of the bidirectional lay-up sequence, the flexural stresses are not continuous through thickness in cross-ply laminates. Figure 12 shows these discontinuities in the long-beam cross-ply laminate in local coordinate system, while Figure 13 shows the through-thickness stress distribution at the centre.

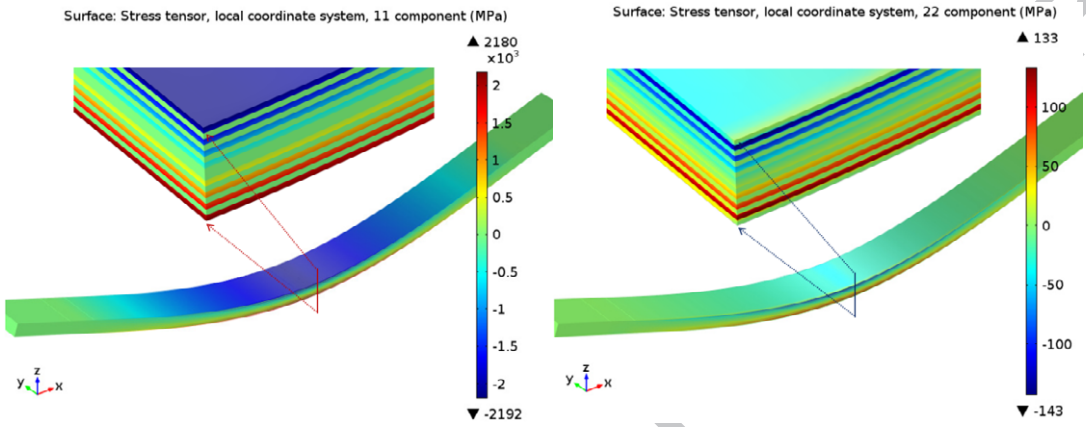

Figure 12 Distributions of stress components c_1 (left) and c_2 (right) in long-beam cross-ply laminate and their side-views.

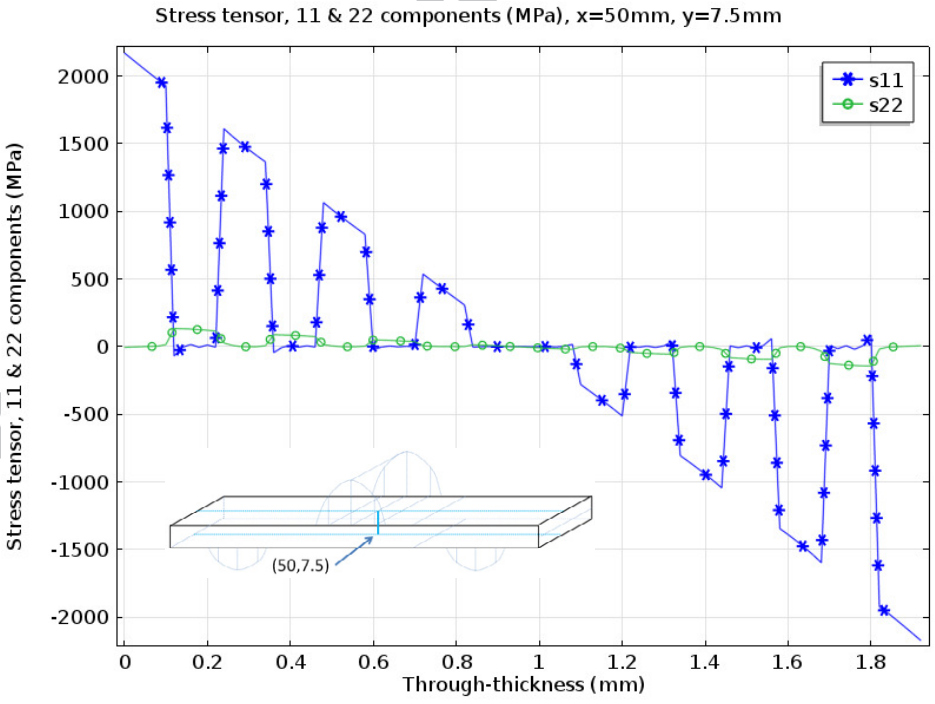

Figure 13 Through-thickness distributions of flexural stress c_1 (s11) and c_2 (s22) at central point of long-beam cross-ply laminate. The stresses jump rapidly at the interface between longitudinal and transverse plies.

Figure 13 shows that the maximum c_1 and c_2 at the centre of laminate are about ±2.2GPa and ±140MPa respectively. A comparison of these values with the lamina strength shown in Table 5 illustrates that the longitudinal compressive stress has exceeded the lamina compressive strength, while the longitudinal tensile stress is slightly lower than lamina tensile strength. In accordance with the experimental condition, the top ply could withstand such high value of compressive stress, because the microbuckling was constrained by the roller and supported by the transverse ply underneath it. In this condition, the top ply would be more difficult to 'buckle' compared to the situation in a unidirectional laminate (c.f. Fig. 9). Figure 14 shows the schematics of fibre orientation in long-beam cross-ply laminate. The out-of-plane buckling of fibres in the top ply is constraint by the roller and the transverse fibres in the adjacent ply. Therefore the compressive strength of the material is significantly improved.

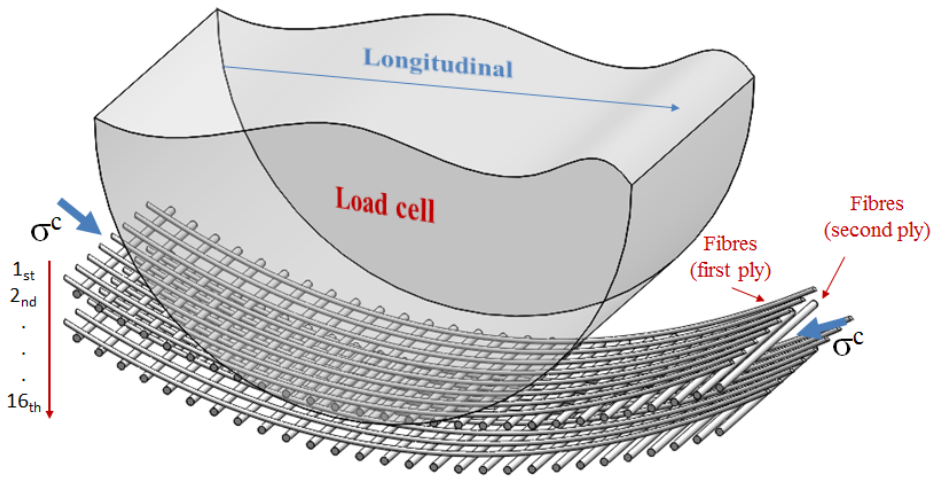

Figure 14 Schematics of fibre microbuckling of long-beam cross-ply laminate. With the support of the second ply, the first ply is more difficult to fail by microbuckling.

On the other hand, it is widely recognized that the plastic matrix could withstand higher compressive stress than tensile stress. Therefore, the 15th ply (90° orientation with low stiffness) in the tensile region was more likely to fail than the second ply (90°) in the compressive region. Indeed, the tensile stress in the 15th ply had exceeded the transverse tensile strength of resin shown in Table 5. Therefore, failure sequence of long-beam cross-ply laminate can be explained as, a) the 15th ply failed in tension and the stiffness had a tiny drop (90° ply failed), b) the 16th ply (0° orientation with high stiffness) delaminated and failed in tension, and then the stiffness shown a huge decrease, c) the delamination propagated inside the laminate and it failed. Figure 15 shows a typical microscope failure image of long-beam

cross-ply laminate, while Figure 16 shows the deflection-load curves of long-beam cross-ply laminate.

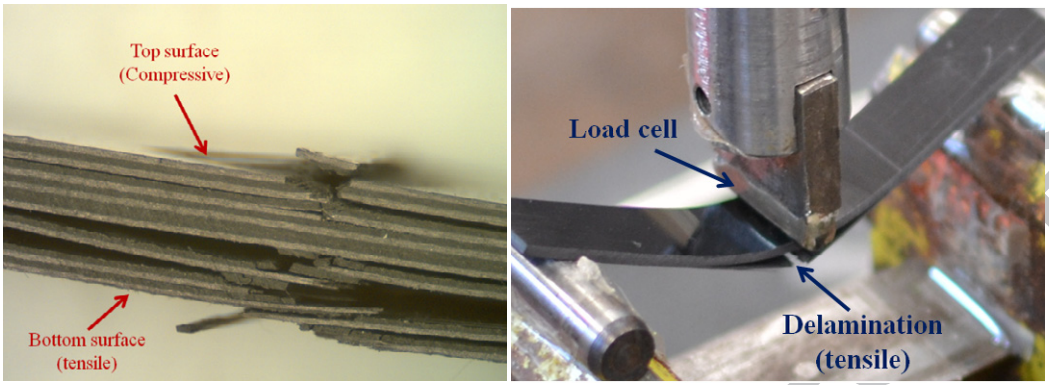

Figure 15 Typical microscope failure image of long-beam cross-ply laminate (left) and its tensile failure in 3-point bending (right).

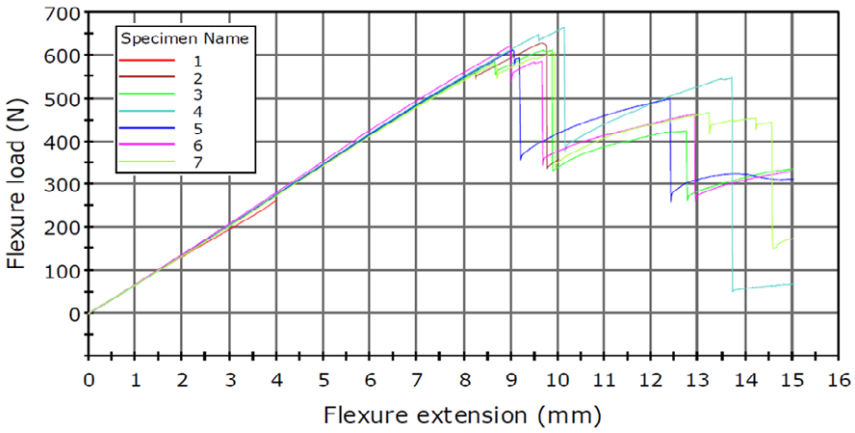

Figure 16 Deflection-load curves of long-beam cross-ply laminate. The small and large 'stiffness losses' represent the failure of transverse and longitudinal plies.

Applying the Tsai-Hill failure criterion to the FEA results of the long-beam cross-ply laminate, indicates that the interlaminar shear stress contributed about 4% to the criterion. However, the stress component c_2 contributes much more due to the lower transverse tensile strength $\left(\sigma_2^{ult}\right)$. Figure 17 shows the distribution of the Tsai-Hill failure criterion in the long-beam cross-ply laminate. The maximum value appeared at the interfaces of the first and second plies corresponding to the maximum transverse stress c_2, as shown in Figure 12. Delamination was also observed between the 1st and the 2nd ply in the experiment as shown in Figure 15.

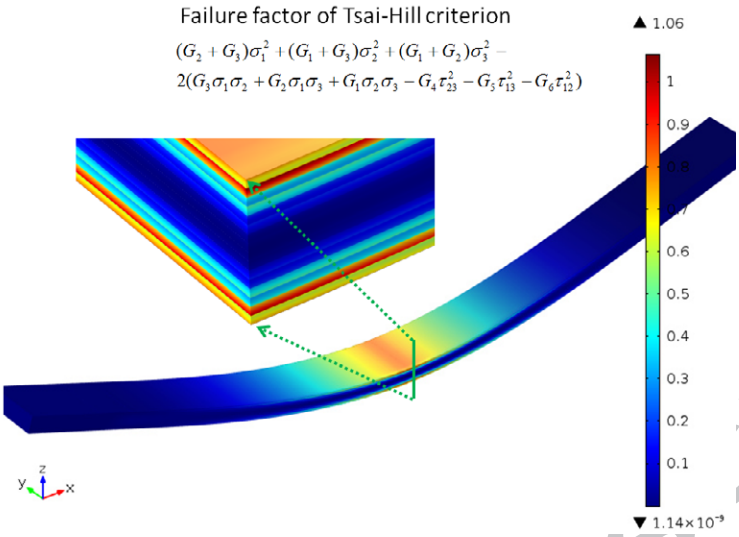

Figure 17 Distribution of Tsai-Hill 'failure factor' in long-beam cross-ply laminate. The transverse plies exceeded the failure criterion rather than the surface plies.

For the short-beam cross-ply laminate, the interlaminar shear stress τ_{13} is not continuous due to the bidirectional lay-up sequence, and the maximum value appears at the interface between the 7th and 8th plies (z=1.08mm) rather than the mid-plane. This is different from the measured apparent interlaminar shear stress (shown in Table 2). Figure 18 shows the distribution of interlaminar shear stress τ_{13} through-thickness at x=13mm. The coordinates are (13, 0), (13, 0.6) and (13, 5) respectively.

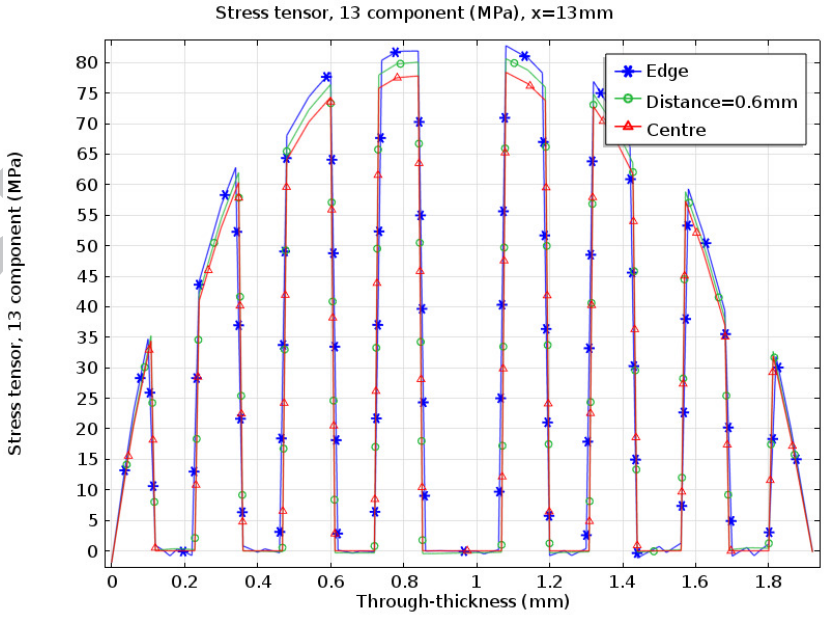

Figure 18 Distribution of interlaminar shear stress τ_{13} of short-beam cross-ply laminate. The free edge effect is slight, compared with short-beam unidirectional laminate.

It can be seen from Figure 18 that the maximum value of τ_{13} is lower than the interlaminar shear strength shown in Table 5. The transverse and out-of-plane components of normal stress, σ_2 and σ_3 are much higher, compared with the short-beam unidirectional laminate. Figure 19 shows the distributions of these two normal stress components in the short-beam cross-ply laminate. The maximum values of σ_2 and σ_3 are so high that they have exceeded the transverse tensile strength $\left(\sigma_2^{ult}\right)$. It indicates that the laminate failed in transverse compression initializing at the second ply. Following the 'stiffness losses' and stresses re-distribution, the maximum interlaminar shear stress τ_{13} exceeded the shear strength, and then the laminate failed. Figure 20 shows a typical microscope image of interlaminar failure of short-beam cross-ply laminate.

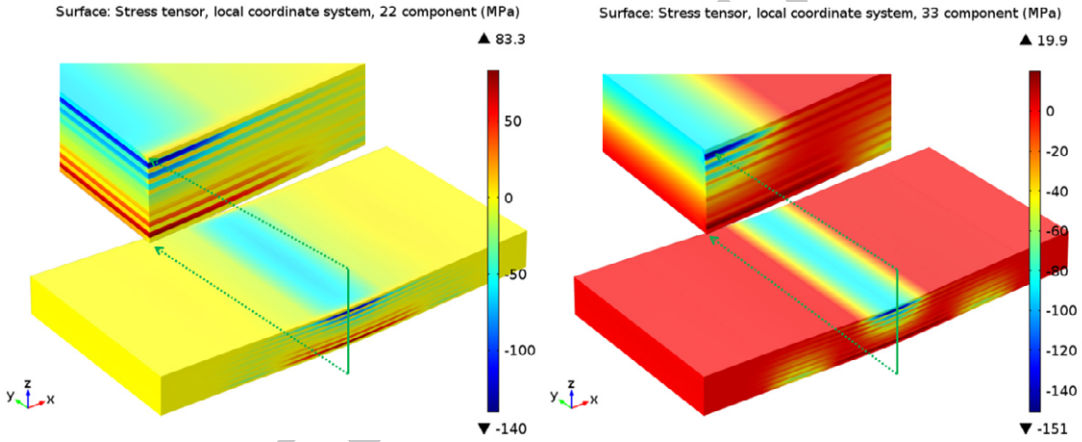

Figure 19 Distributions of normal stress σ_2 (left) and σ_3 (right) in short-beam cross-ply laminate and their side-views. The maximum stresses appeared at the second ply (90°), and strong free edge effect on σ_3 is observed.

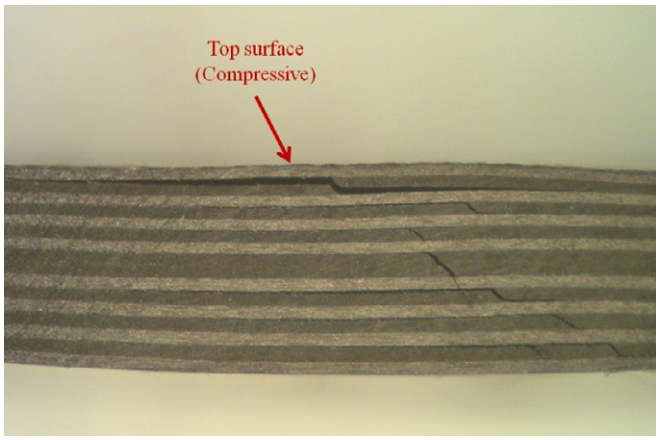

Figure 20 Typical microscope failure image of short-beam cross-ply laminate. The initial delamination began from the 2nd ply, corresponding to the maximum σ_2 and σ_3 in Figure 19.

5.3 Angle-ply laminate

For the angle-ply laminate, the distributions of these flexural stresses are quite different from the symmetric laminates. Moreover, the CLT and 3D FEA models present significantly different results. With the infinite plane hypothesis, the CLT method provides a relative smooth distribution of stresses. Figure 21 shows the distribution of interlaminar shear stress τ_{xz} (global) and τ_{13} (local) through-thickness in short-beam angle-ply laminate, evaluated by CLT method. It can be seen that both of the maximum value of τ_{xz} and τ_{13} appear at the mid-plane (z=0.92mm), and the shear stress τ_{13} in local coordinate system is not continuous because of the complicated lay-up sequence.

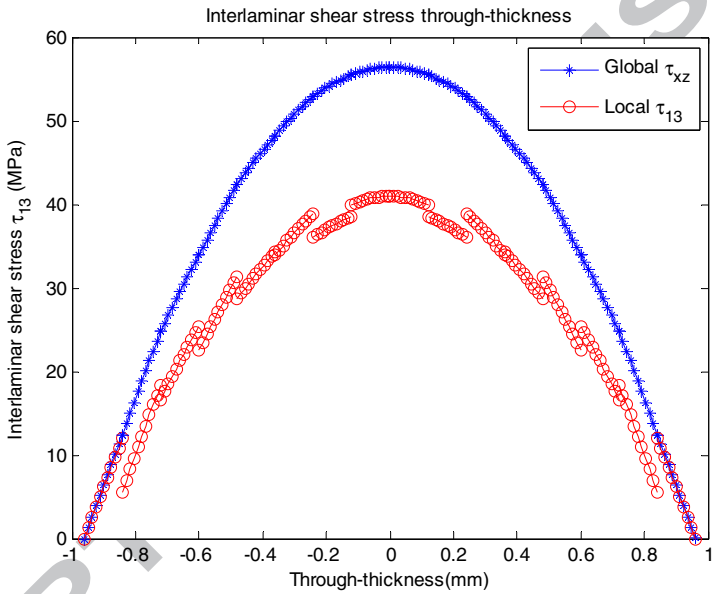

Figure 21 Interlaminar shear stress τ_{xz} and τ_{13} distribution through-thicknesses in short-beam angle-ply laminate (CLT). The discrete τ_{13} represents the complicated lamina orientation.

The curves extracted from the CLT method show that the local interlaminar shear stress τ_{13} is lower than the global value. Furthermore, these curves are so uniform that they provide no information about the free edge effects.

The early works of Pipes and Pagano [10, 11] had predicted the singularity of interlaminar shear stress near the free edge region of a $[\pm 45°]_2$ angle-ply laminate under axial load. 3D FEA models in the present work also show the increase of interlaminar shear stress in the short-beam angle-ply laminate under bending. Figure 22 shows the through-thickness distribution of interlaminar shear stress of the short-beam angle-ply laminate. It can be seen

that both the τ_{xz} and τ_{13} near free edge area fluctuate remarkably. The maximum values appear at the interface between the 4th and 5th plies, instead of the mid-plane (8th and 9th plies, as predicted by CLT, shown in Figure 21). However, the distribution tends to be uniform inside the laminate. A small distance from the edge (2 ply-thicknesses, 0.24mm), the distribution of global shear stress τ_{xz} becomes a parabolic shape, while the maximum value of local shear stress τ_{13} at the mid-plane drops approximate 20%. Finally both of the global and local shear stresses converge to the CLT at central area.

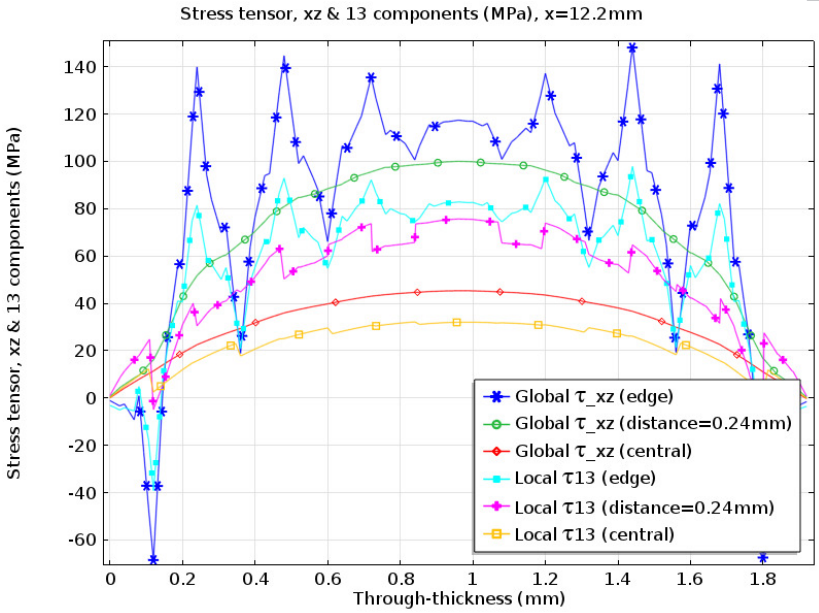

Figure 22 Distributions of interlaminar shear stress through-thicknesses in short-beam angle-ply (3D FEA model). The 'stress peaks' at edge area converge to CLT at centre, and the maximum value appears at z=1.44mm (interface of 4-5 plies).

This extremely high global shear stress τ_{xz} at the free edge located at the interface of two plies, which may lead to delamination, while the local shear stress τ_{13} at the corresponding location is very close to the shear strength τ_{13}^{ult} shown in Table 5. Moreover, quite a few points with these 'extreme values' can be found at the interface of two plies, which are easier to induce the 'multi-crack' at the edge area. Figure 23 shows the surface plot and slice plot of local shear stress τ_{13} of the short-beam angle-ply laminate, while Figure 24 shows the diagram of the free edge effect.

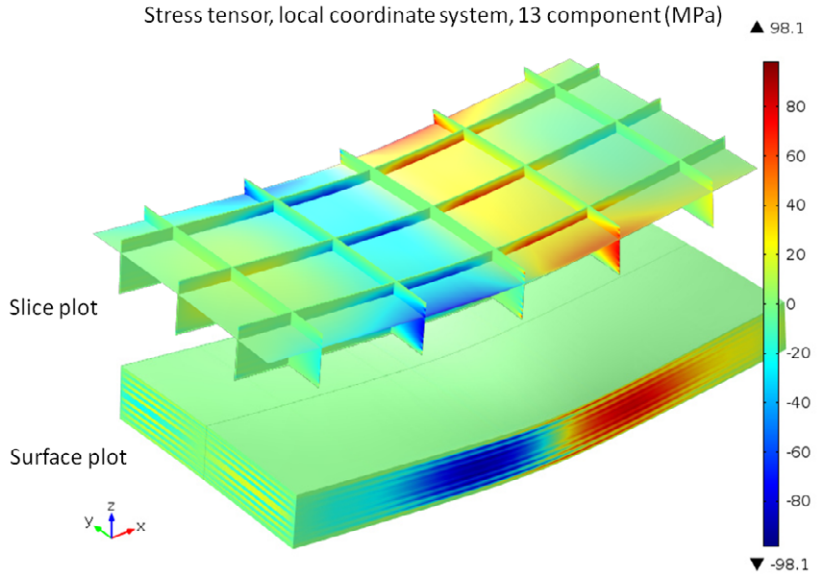

Figure 23 3D distribution of τ_{13} in short-beam angle-ply laminate. The slice plot reveals the distribution of τ_{13} in 3D scale, and the surface plot shows the variation of τ_{13} in different plies with particular fibre orientation.

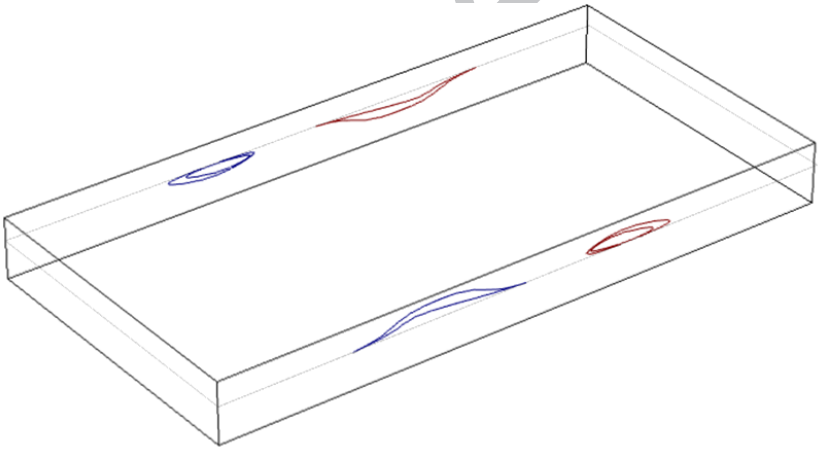

Figure 24 Contour curves of interlaminar shear stress τ_{13} in short-beam angle-ply laminate (z=1.44mm). The extremely high stress only appears near the edge area.

It should be noted that the interaction ratio (η_{xyx}) between normal stress σ_x and in-plane shear stress τ_{xy} is too high to be neglected in angle-ply laminates. According to 3D CLT (shown in Appendix II), the transformed compliance matrix $\overline{S}$ of angle-ply laminate shows non-zero 'interaction' terms ($\overline{S_{16}}$ and $\overline{S_{26}}$), leading to a definition of interaction ratios:

$$\eta_{xyx} = E_x \overline{S_{16}}$$
$$\eta_{xyy} = E_x \overline{S_{26}} \qquad (10)$$

The interaction ratio (η_{xyx}) represents the ratio of the shear strain γ_{xy} induced by normal stress σ_x, to the normal strain ε_x induced by the same normal stress σ_x.

Figure 25 shows the relationship between interaction ratio η_{xyx} and the off-axis angle (predicted by CLT). The interaction ratio (η_{xyx}) evaluated by CLT predicted a value of about -0.7 in angle-ply lamina (45°). It illustrates the axial stress could induce rather high in-plane shear stress, which is happening in the present case of the short-beam angle-ply laminate. The authors found that for many commercial CFRP composites, the maximum value of interaction ratio appears around 10-13° off-axis angle. Table 7 shows the maximum interaction ratio of ten commercial CFRP composites. In Table 7, there are ten different commercial CFRP composites and their maximum interaction ratios are very close. In fact, the coefficient of variation of off-axis angle is 1.3%.

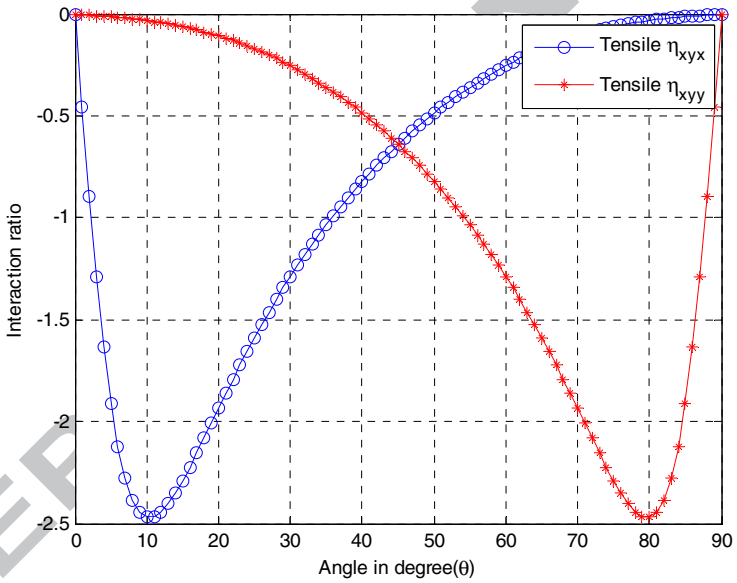

Figure 25 Interaction between axial stress and shear stress in off-axis laminate (according to CLT). The value of η represents the couple of normal stress to shear stress.

Due to the complex structure in angle-ply laminate, the interaction ratio (η) strongly affects the distribution of the in-plane shear stress τ_{xy} in 3D. Indeed, the value of in-plane shear stress τ_{xy} is much higher than the other two shear stress components τ_{xz} and τ_{yz}. Because of the nature of three-point bending, the maximum normal stress appears at the top and bottom plies. As a consequence, this 'induced' in-plane shear stress τ_{xy} may lead to strong twisting at

the two surfaces of the laminate. Figure 26 shows the slice plot and surface plot of in-plane shear stress τ_{12} in short-beam angle-ply laminate.

Table 7 Engineering constants[44] and the interaction ratio (according to CLT)

	$E_1(GPa)$	$E_2(GPa)$	ν_{12}	$G_{12}(GPa)$	$\left\|\eta_{xyx}^{\max}\right\|$	$\theta(^\circ)$
IM7/977-3	191	9.94	0.35	7.79	2.259	12
T800/Cytec	162	9	0.4	5	2.622	10
T700 C-Ply 55	121	8	0.3	4.7	2.301	11
T700 C-Ply 64	141	9.3	0.3	5.8	2.224	12
AS4/H3501	138	8.96	0.3	7.1	1.970	13
IM6/epoxy	203	11.2	0.32	8.4	2.237	12
AS4/F937	148	9.65	0.3	4.55	2.625	10
T300/N5208	181	10.3	0.28	7.17	2.288	12
IM7/8552	171	9.08	0.32	5.29	2.629	10
IM7/MTM45	175	8.2	0.33	5.5	2.616	10
Average	163.1	9.363	0.32	6.13	2.377	11.2
SDs	25.85	0.96	0.03	1.37	0.23	1.14
Coeff var	15.9%	10.2%	10.7%	22.4%	9.7%	1.3%*

***Divided by 90°**

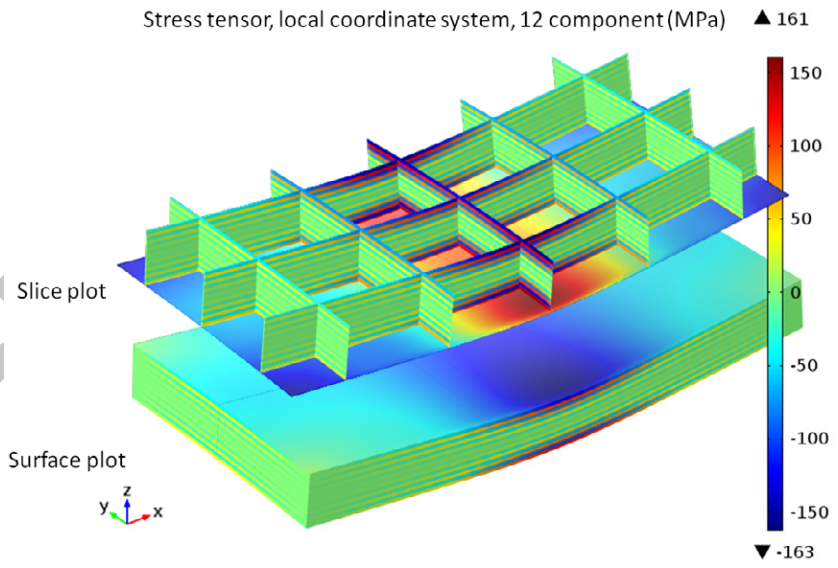

Figure 26 Slice plot (upper) and surface plot (lower) of in-plane shear stress in short-beam angle-ply laminate. The values of τ_{12} near the middle area of top and bottom surfaces are so high that strong distortion was observed in the bending test.

The observation of microscope images confirmed the results from 3D FEA models. Instead of delamination failure (as likely occurred in unidirectional and cross-ply laminates), the failure mode in angle-ply laminate was the combination of in-plane shear stress τ_{12} and interlaminar shear stress τ_{13}. Consequently, the crack appeared near the two free edge sides of specimen, but without propagating through the whole width. Figure 27 gives a typical microscope failure image of short-beam angle-ply specimen under three-point bending, while Figure 28 shows the deflection-load curves.

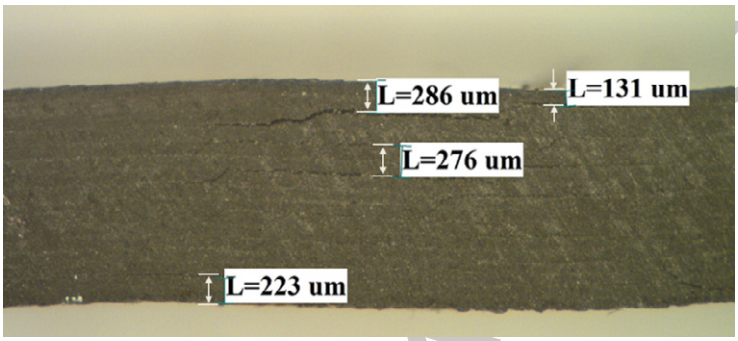

Figure 27 Typical failure image of angle-ply laminate under bending test condition. Cracks appeared at free edge area, but without penetrating inside the volume. The positions of cracks correspond to a peak of interlaminar shear stress, as shown in Figure 22. Specimen twisting induced by in-plane shear stress was observed.

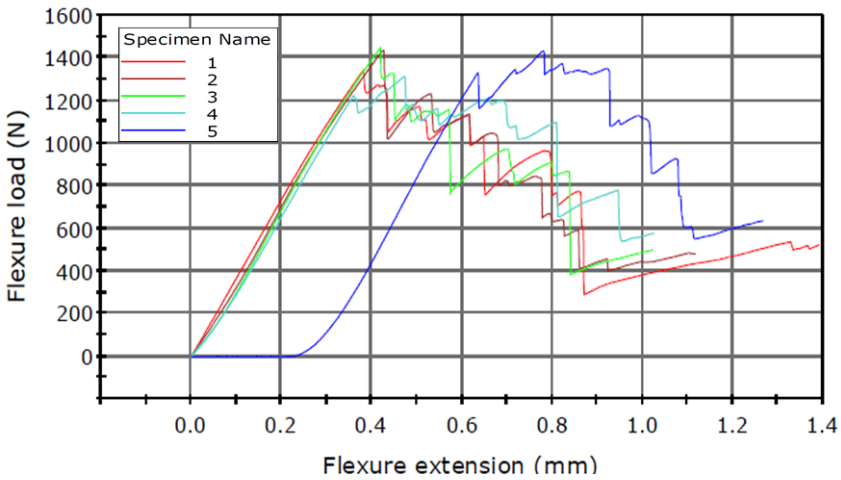

Figure 28 Deflection-load curves in angle-ply laminate from three-point bending test. Each crack represented a 'stiffness losses' in bending test.

6. Conclusions

In bending, composite laminates are subjected to both tension and compression, which is fundamentally different from uniaxial loadings. This study has illustrated, by means of 3D FEA, 3D CLT and experiments, that all six stress components make contribution to the failure

modes in the respective laminates. Three lay-up sequences were considered to cover the typical conditions of composite laminates. Compared with shell approximations, 3D FEA is capable of modelling laminated composites with arbitrary lay-ups, and provides more accurate results. It has been shown that the combination of these three approaches can reveal the initiation of failure of composite laminates; used in isolation, the approaches are unlikely to be successful.

Study of the different failure mechanisms indicates ways in which laminate design might be improved. The unidirectional laminate failed in compression (fibre microbuckling); however with the support of the lower transverse ply, the longitudinal ply in the cross-ply laminate was more difficult to buckle, and as a consequence it could withstand a much higher compressive stress. This indicates that for practical composite structures, inserting a transverse ply into a unidirectional laminate (such as $[0/90/0_n]$) could significantly improve the bending performance.

It has been shown that the in-plane shear stress in angle-ply laminate is much higher than the interlaminar shear stress, and this leads to laminate twisting under bending loads. However, this stress component has been neglected by many previous studies. This study also shows that the maximum interaction ratio appears at around 10°-13° off-axis, therefore suggested that these orientations should be avoided in the surface plies of practical composite laminates.

It has also been demonstrated that the free edge effects are strongly dependent on the laminate lay-up and loading span. The asymmetric laminate (angle-ply) presents much more significant free edge effects than symmetric laminates (unidirectional and cross-ply), while these effects are more significant in short span loading. Meanwhile, the free edge effects decay inside the laminate much more rapidly in the asymmetric laminate compared to symmetric laminates. The stress components of all laminates converge to the value predicted by CLT in central area.

7. Acknowledgements

The authors would like to thank Professor Long-yuan Li for his advice on FEA modelling, Dr Richard Cullen for his kind help with composites manufacturing, Terry Richards for his support of the mechanical tests, and the financial support of the School of Marine Science and Engineering, Plymouth University.

References

1. Brøndsted, P., H. Lilholt, and A. Lystrup, *Composite materials for wind power turbine blades.* Annu. Rev. Mater. Res., 2005. **35**: p. 505-538.
2. Mohan, M., *The advantages of composite materials in marine renewable energy structures.* RINA Marine Renewable Energy Conference 2008 2008.
3. Granata, R.D., et al., *Durability of Composite Materials and Structures*, 2009, DTIC Document.
4. Kaw, A.K., *Mchanics of composite materials (second edition).* Taylor & Francis Group, 2006(ISBN 0-8493-1343-0).
5. Yang, P.C., C.H. Norris, and Y. Stavsky, *Elastic wave propagation in heterogeneous plates.* International Journal of Solids and Structures, 1966. **2**(4): p. 665-684.
6. Whitney, J. and N. Pagano, *Shear deformation in heterogeneous anisotropic plates.* Journal of Applied Mechanics, 1970. **37**(4): p. 1031-1036.
7. Jing, H.-S. and K.-G. Tzeng, *Refined shear deformation theory of laminated shells.* AIAA journal, 1993. **31**(4): p. 765-773.
8. Pagano, N. and J. Halpin, *Influence of end constraint in the testing of anisotropic bodies.* Journal of Composite Materials, 1968. **2**(1): p. 18-31.
9. Puppo, A. and H. Evensen, *Interlaminar shear in laminated composites under generalized plane stress.* Journal of composite materials, 1970. **4**(2): p. 204-220.
10. Pipes, R.B. and N.J. Pagano, *Interlaminar Stresses in Composite Laminates Under Uniform Axial Extension.* Journal of Composite Materials, 1970. **4**: p. 11.
11. Pagano, N., *Stress fields in composite laminates.* International Journal of Solids and Structures, 1978. **14**(5): p. 385-400.
12. Wang, A. and F.W. Crossman, *Some new results on edge effect in symmetric composite laminates.* Journal of Composite Materials, 1977. **11**(1): p. 92-106.
13. Kassapoglou, C., *Determination of interlaminar stresses in composite laminates under combined loads.* Journal of reinforced plastics and composites, 1990. **9**(1): p. 33-58.
14. Murthy, P.L. and C.C. Chamis, *Free-edge delamination: laminate width and loading conditions effects.* 1987.
15. Pipes, R.B., *Boundary layer effects in composite laminates.* Fibre Science and Technology, 1980. **13**(1): p. 49-71.
16. Wang, S. and I. Choi, *Boundary-layer effects in composite laminates: Part 2—free-edge stress solutions and basic characteristics.* Journal of Applied Mechanics, 1982. **49**(3): p. 549-560.
17. Tang, S., *A boundary layer theory-Part I: Laminated composites in plane stress.* Journal of composite materials, 1975. **9**(1): p. 33-41.
18. Tang, S. and A. Levy, *A boundary layer theory-part II: extension of laminated finite strip.* Journal of Composite Materials, 1975. **9**(1): p. 42-52.
19. Lee, C. and J. Chen, *Interlaminar shear stress analysis of composite laminate with layer reduction technique.* International journal for numerical methods in engineering, 1996. **39**(5): p. 847-865.
20. Kant, T. and K. Swaminathan, *Estimation of transverse/interlaminar stresses in laminated composites–a selective review and survey of current developments.* Composite structures, 2000. **49**(1): p. 65-75.
21. Foye, R. and D. Baker. *Design of orthotropic laminates*. in *11th Annual AIAA Structures, Structural Dynamics, and Materials Conference, Denver, Colorado*. 1970.
22. ISO, I., *14125: 1998 (E).* Fibre reinforced plastic composites–determination of flexural properties, 1998.
23. ISO, B., *14130.* Fibre-Reinforced Plastic Composites—Determina tion of Apparent Interlaminar Shear Strength by Short-Beam, 1998.
24. 14125, I., *Fibre-reinforced plastic composites— Determination of flexural properties*, in *ISO standard*1998.

25. 14130, I., *Fibre-reinforced plastic composites—Determination of apparent interlaminar shear strength by short-beam method*, in *ISO standard*1998.
26. Cytec, *CYCOM 977-2 Epoxy resin system. www.cytec.com.* Technical data sheet, 2012.
27. Tenax, T., *Toho Tenax HTS. www.tohotenax-eu.com.* Technical data sheet.
28. Bowles, D.E. and S.S. Tompkins, *Prediction of coefficients of thermal expansion for unidirectional composites.* Journal of Composite Materials, 1989. **23**(4): p. 370-388.
29. Voyiadjis, G.Z. and P.I. Kattan, *Mechanics of Composite Materials with MATLAB.* 2005(Springer).
30. Hyer, M.W., *Stress analysis of fiber-reinforced composite materials*. 2009: DEStech Publications, Inc.
31. Hull, D. and T. Clyne, *An introduction to composite materials*. 1996: Cambridge university press.
32. Halpin, J.C. and J.L. Kardos, *The Halpin-Tsai equations: A review.* POLYMER ENGINEERING AND SCIENCE, 1976. **16**(5): p. 9.
33. Tsai, S.W., *Strength theories of filamentary structures.* Fundamental aspects of fiber reinforced plastic composites, 1968: p. 3-11.
34. Gibson, R.F., *Principles of composite materials mechanics.* McGraw-Hill, 1994(ISBN O-07-023451-5).
35. Berbinau, P., C. Soutis, and I. Guz, *Compressive failure of 0 unidirectional carbon-fibre-reinforced plastic (CFRP) laminates by fibre microbuckling.* Composites Science and technology, 1999. **59**(9): p. 1451-1455.
36. COMSOL, *COMSOL Multiphysics reference manual.* 2013.
37. Creemers, R., *Interlaminar shear strength criteria for composites.* 2009.
38. MATWORKS, *MATLAB reference manual.* 2013.
39. Budiansky, B. and N.A. Fleck, *Compressive failure of fibre composites.* Journal of the Mechanics and Physics of Solids, 1993. **41**(1): p. 183-211.
40. Soutis, C., *Compressive strength of unidirectional composites: measurement and prediction.* ASTM special technical publication, 1997. **1242**: p. 168-176.
41. Soutis, C., *Measurement of the static compressive strength of carbon-fibre/epoxy laminates.* Composites science and technology, 1991. **42**(4): p. 373-392.
42. Liu, D., N. Fleck, and M. Sutcliffe, *Compressive strength of fibre composites with random fibre waviness.* Journal of the Mechanics and Physics of Solids, 2004. **52**(7): p. 1481-1505.
43. Lemanski, S.L., et al., *Modelling failure of composite specimens with defects under compression loading.* Composites Part A: Applied Science and Manufacturing, 2013. **48**(0): p. 26-36.
44. Tsai, S.W. and J.D.D. Melo, *An invariant-based theory of composites.* Composites Science and Technology, 2014. **100**: p. 237-243.
45. Lekhnitskiĭ, S., *Theory of elasticity of an anisotropic elastic body*. 1963: Holden-Day.

Appendix I: calculation of Poisson's ratio ν_{23}

In the present work, the transverse Poisson's ratio was derived by hydrostatic assumption. Considering a bulk material under hydrostatic pressure, the change of volume is equal to the summary of three strain vectors,

$$\Delta V = c \ / K = \varepsilon_1 + \varepsilon_2 + \varepsilon_3 \tag{11}$$

Substituting the orthotropic properties ($E_2 = E_3, G_{12} = G_{13}, \nu_{12} = \nu_{13}$) into the relation of stress and strain,

$$\begin{bmatrix} \varepsilon_1 \\ \varepsilon_2 \\ \varepsilon_3 \end{bmatrix} = \begin{bmatrix} 1/E_1 & -\nu_{21}/E_2 & -\nu_{31}/E_3 \\ -\nu_{12}/E_1 & 1/E_2 & -\nu_{32}/E_3 \\ -\nu_{13}/E_1 & -\nu_{23}/E_2 & 1/E_3 \end{bmatrix} \begin{bmatrix} \sigma_1 \\ \sigma_2 \\ \sigma_3 \end{bmatrix} \tag{12-1}$$

$$\varepsilon_1 + \varepsilon_2 + \varepsilon_3 = \sigma \left[\frac{1-2\nu_{12}}{E_1} + \frac{2(1-\nu_{21}-\nu_{23})}{E_2} \right] \tag{12-2}$$

The transverse Poisson's ratio can be calculated by bulk modulus, while the bulk modulus is calculated by Halpin-Tsai empirical equation,

$$\nu_{23} = 1 - \nu_{21} - \frac{E_2}{2K} + \frac{E_2(1 - 2\nu_{12})}{2E_1} \tag{13}$$

$$K = \frac{K_m(1 + \zeta\eta V_f)}{1 - \eta V_f}$$
$$\eta = \frac{K_f/K_m - 1}{K_f/K_m + \zeta} \tag{14}$$

Appendix II: 3D CLT formulae

With respect to the material symmetry, the composite compliance matrix S is reduced to an orthotropic matrix. Applying the well-known stiffness transformation law [45], the off-axis compliance matrix $\overline{S}$ and stiffness matrix $\overline{C}$ in 3D scale can be extended as,

$$\begin{aligned} \overline{S} &= T_{\varepsilon}^{-1} S T_{\sigma} \\ \overline{C} &= \left[\overline{S}\right]^{-1} \end{aligned} \tag{15}$$

$$S = \begin{bmatrix} 1/E_1 & -\nu_{12}/E_1 & -\nu_{12}/E_1 & 0 & 0 & 0 \\ -\nu_{12}/E_1 & 1/E_2 & -\nu_{23}/E_2 & 0 & 0 & 0 \\ -\nu_{12}/E_1 & -\nu_{23}/E_2 & 1/E_2 & 0 & 0 & 0 \\ 0 & 0 & 0 & 1/G_{23} & 0 & 0 \\ 0 & 0 & 0 & 0 & 1/G_{12} & 0 \\ 0 & 0 & 0 & 0 & 0 & 1/G_{12} \end{bmatrix} \tag{16}$$

$$T_{\varepsilon} = \begin{bmatrix} c^2 & s^2 & 0 & 0 & 0 & cs \\ s^2 & c^2 & 0 & 0 & 0 & -cs \\ 0 & 0 & 1 & 0 & 0 & 0 \\ 0 & 0 & 0 & c & s & 0 \\ 0 & 0 & 0 & -s & c & 0 \\ -2cs & 2cs & 0 & 0 & 0 & c^2 - s^2 \end{bmatrix} \tag{17}$$

$$T_{\sigma} = \begin{bmatrix} c^2 & s^2 & 0 & 0 & 0 & 2cs \\ s^2 & c^2 & 0 & 0 & 0 & -2cs \\ 0 & 0 & 1 & 0 & 0 & 0 \\ 0 & 0 & 0 & c & s & 0 \\ 0 & 0 & 0 & -s & c & 0 \\ -cs & cs & 0 & 0 & 0 & c^2 - s^2 \end{bmatrix} \tag{18}$$

where S is the compliance matrix of lamina; $c = \cos(\theta)$ and $s = \sin(\theta)$.

Substituting the three-dimensional version of composites compliance matrix into CLT equations [4], the three-dimensional version of [A], [B] and [D] matrices can be written as,

$$[A]=\sum_{k=1}^{N}\left(\overline{C}_{ij}\right)_k\left(z_k-z_{k-1}\right)$$
$$[B]=\frac{1}{2}\sum_{k=1}^{N}\left(\overline{C}_{ij}\right)_k\left(z_k^2-z_{k-1}^2\right) \quad (19)$$
$$[D]=\frac{1}{3}\sum_{k=1}^{N}\left(\overline{C}_{ij}\right)_k\left(z_k^3-z_{k-1}^3\right)$$

Assembling the [A], [B] and [D] matrices for $\begin{bmatrix} A & B \\ B & D \end{bmatrix}$ matrix, and its inversed $\begin{bmatrix} a & b \\ b & d \end{bmatrix}$ matrix,

$$\begin{bmatrix} N \\ M \end{bmatrix}=\begin{bmatrix} A & B \\ B & D \end{bmatrix}\begin{bmatrix} \varepsilon \\ \kappa \end{bmatrix} \quad (20\text{-}1)$$

$$[A,B;B,D]=\begin{bmatrix} A & B \\ B & D \end{bmatrix} \quad (20\text{-}2)$$

$$[a,b;b,d]=\begin{bmatrix} a & b \\ b & d \end{bmatrix}=\begin{bmatrix} A & B \\ B & D \end{bmatrix}^{-1} \quad (20\text{-}3)$$

Once the three-dimensional $[a,b;b,d]$ matrix is assembled, the flexural modulus of laminate can be evaluated by [4],

$$E_{CLT}^{f}=\frac{12}{h^3 d_{11}} \quad (21)$$

Consider a composite laminate with symmetric lay-up pattern under three-point bending condition, the coupling matrix $[B]=0$, the moment about x axes can be written as,

$$M_x=\frac{\kappa_x}{d_{11}}=\frac{FL}{4w} \quad (22)$$

If it is assumed that the curvature through-thickness is a constant, the strain and longitudinal stress are determined by,

$$\varepsilon_x^z=z\kappa_x=\frac{zFLd_{11}}{4w}$$
$$\sigma_1^z=E_k\varepsilon_x^z=E_k\frac{zFLd_{11}}{4w} \quad (23)$$

The maximum strain appears on the top and bottom surfaces $z = \pm\frac{h}{2}$. However, the maximum stress is dependent on both the through-thickness coordinate and the ply modulus. The CLT formulae in the present work were solved by MATLAB.

Nomenclature

$[a],[b],[d]$	Block matrices of $\begin{bmatrix} a & b \\ b & d \end{bmatrix}$ matrix (inversed $\begin{bmatrix} A & B \\ B & D \end{bmatrix}$ matrix)
r_1, r_2	Radius of load cell and support rollers
q	Mesh quality factor
w, h, l	Width, height and length of laminate
$[A],[B],[D]$	Block matrices of $\begin{bmatrix} A & B \\ B & D \end{bmatrix}$ matrix
$\overline{C}$	Off-axis stiffness matrix of lamina
$\left(\overline{C_{ij}}\right)_k$	Off-axis stiffness matrix of the k^{th} ply
$D_{\max}$	Maximum deflection
E_{app}^f	Apparent flexural modulus
E_{CLT}^f, E_x^f	Flexural modulus evaluated by CLT
E_1^f, E_2^f, E_3^f	Principal elastic moduli of fibre
E_1, E_2, E_3	Principal elastic moduli of lamina
E_m	Elastic modulus of matrix
$F_{\max}$	Maximum flexure force
$G_{12}^f, G_{23}^f, G_{13}^f$	Principal shear moduli of fibre
G_{12}, G_{23}, G_{13}	Principal shear moduli of lamina
G_m	Shear moduli of matrix
I	Moment of inertia

K, K_f, K_m	Bulk moduli of lamina, fibre and matrix
L	Span
M, M_x	Moment
$N_{x,y,xy}, M_{x,y,xy}$	Force and moment per unit length
P	Sinusoidal pressure
$Q_{ij}, \overline{Q}_{ij}$	Extensional compliance matrix of unidirectional and off-axis lamina
Q_x	Force per unit length along the width
S	Compliance matrix of lamina
$\overline{S}$	Off-axis compliance matrix of lamina
T_ε, T_σ	Transformation matrices of strain and stress
V_f	Fibre volume fraction
V	Volume of a mesh element
W_m	Matrix fraction in weight
γ_{xy}	In-plane shear strain
ε	Normal strain
ζ	Halpin-Tsai adjusted parameter, for rectangle section $\zeta = 1$
η_{xyx}, η_{xyy}	Interaction ratio
θ	Angle
κ	Curvature
$\nu_{12}, \nu_{23}, \nu_{13}$	Principal Poisson's ratios of lamina
$\nu_{12}^f, \nu_{23}^f, \nu_{13}^f$	Principal Poisson's ratios of fibre

ν_m	Poisson's ratio of matrix
π	Circumference ratio
λ_0	Half-wavelength of fibres microbuckling
c_1, c_2, c_3	Normal stress in local coordinate system
c_x, c_y, c_z	Normal stress in global coordinate system
$\left(\sigma_1^{ult}\right)^t, \left(\sigma_2^{ult}\right)^t$	Principal tensile strength of lamina
$\left(\sigma_1^{ult}\right)^c$	Longitudinal compressive strength of lamina
$\left(\sigma_2^{ult}\right)^f$	Transverse flexural strength of lamina
$\left(\sigma_f^{ult}\right)^t$	Ultimate tensile strength of fibre
$\left(\sigma_m^{ult}\right)^t, \left(\sigma_m^{ult}\right)^f$	Ultimate tensile and flexural strength of matrix
$\tau_{12}, \tau_{13}, \tau_{23}$	Shear stress in local coordinate system
$\tau_{12}^{ult}, \tau_{23}^{ult}, \tau_{13}^{ult}$	Shear strength of lamina
$\tau_{xy}, \tau_{xz}, \tau_{yz}$	Shear stress in global coordinate system